



Synergistic effects of Bi₂O₃ and Ta₂O₅ for efficient electrochemical production of H₂O₂

Chenghang Jiang^{a,1}, Yan-Fei Fei^{b,1}, Weiwei Xu^a, Zhikang Bao^a, Yizhen Shao^a, Shijie Zhang^{a,*}, Zhong-Ting Hu^{b,*}, Jianguo Wang^{a,*}

^a Institute of Industrial Catalysis, State Key Laboratory Breeding Base of Green-Chemical Synthesis Technology, College of Chemical Engineering, Zhejiang University of Technology, Hangzhou 310014, PR China

^b College of Environment, Zhejiang University of Technology, Hangzhou 310032, PR China

ARTICLE INFO

Keywords:

Ta₂O₅
Bi₂O₃
Synergistic effect
Hydrogen peroxide
Disinfection

ABSTRACT

Electrochemical oxygen reduction reaction (ORR) through a two-electron pathway has been provided a green route for on-site hydrogen peroxide (H₂O₂) production. Developing high-selective electrocatalysts for H₂O₂ production are urgently sought. Herein, a m-Bi₂O₃/Ta₂O₅ electrocatalyst (m: “Bi” mass contents) has been successfully synthesized by simple physical mixing associated with an outstanding selectivity towards H₂O₂ (94.7%), over 10% higher than Ta₂O₅ (80.9%) and Bi₂O₃ (81.7%). 10-Bi₂O₃/Ta₂O₅ also exhibits 471 mmol/(g_{cat}·h) H₂O₂ yield with 91.8% Faraday Efficiency. The in-situ generated H₂O₂ can function as disinfection agent for efficiently deactivating model bacteria (e.g., *Pseudomonas aeruginosa*, *Staphylococcus aureus* and *Escherichia coli*) within 30 min. In-situ Raman and DFT proposed the synergistic effects of Bi₂O₃ and Ta₂O₅ in boosting 2e⁻ ORR performance. In this work, it not only presents a high-selective electrocatalyst for 2e⁻ ORR, but also provides a new idea for electrocatalyst design from the perspective of reaction process.

1. Introduction

Hydrogen peroxide (H₂O₂) is widely used as an environment-friendly oxidant and disinfectant in diverse industries [1–3], the demand for H₂O₂ gets further increase due to such a severe epidemic. Nowadays, high-concentrations H₂O₂ solution (about 35 wt%) is mainly produced by energy-intensive anthraquinone method [4,5], but the use of noble metal catalysts and costly post-treatment of H₂O₂ products drives us to find a more economical and green way to instead anthraquinone method. Direct synthesis of H₂O₂ (DSHP) from H₂ and O₂ is regarded as an environment-friendly route at low temperatures. The Pd-based catalysts (Pd/TiO₂ [6], FePd/GR-H [7], Au-Pd/SBA-15 [8], Pd/PAH-K2621 [9] et al.) have proven to be effective DSHP catalysts from both experimental and theoretical perspectives. Nevertheless, the industrialization of the DSHP suffers from a variety of challenges, such as explosion and product decomposition. In fact, low-concentrations H₂O₂ solution (about 3 wt%) is sufficient for most applications which brings us to the field of electrocatalysis [10]. Compared to anthraquinone method, two-electron oxygen reduction reaction (2e⁻ ORR) provides a pathway

for on-site production of H₂O₂, and with the only H₂O as byproduct, suggesting the electrocatalytic production of H₂O₂ is relatively cleaner and cheaper. Renewable sources such as wind and solar energy are also very suitable for the electricity supply [11], so it can be foreseen that the application of electrocatalytic H₂O₂ production is very promising.

However, with the presence of 4e⁻ ORR competitive reaction, designing highly selective electrocatalysts towards 2e⁻ ORR remains a challenge. Noble metal catalysts attract much attention due to their fabulous performance in 2e⁻ ORR (Pd/TiO₂ [12], PdAu nanoframe [13]), but the high cost and the complex synthesis process become limiting factors for the practical application of noble metal catalysts. Carbon-based materials show great research value due to their perfect conductivity and high surface area, varieties of carbon-based electrocatalysts (RP/GCN [14], N,O-CNTs [15], B/N-HCNS@VO-G [16], N-CBMC-500 [17], etc.) are reported with superior 2e⁻ ORR performance. Unfortunately, carbon-based catalysts suffer from parasitic oxidation to CO₂ (as the cathode) which leads to performance degradation [18]. Recent researchers also demonstrate that metal oxides also have good electrocatalytic activity for H₂O₂ production. Peng et al. [19]

* Corresponding authors.

E-mail addresses: zjtzsj@163.com (S. Zhang), zthu@zjut.edu.cn (Z.-T. Hu), jgw@zjut.edu.cn (J. Wang).

¹ Chenghang Jiang, Yan-Fei Fei contributed equally to this work

report a Nb₂O₅ catalyst (about 93.4% high selectivity towards 2e⁻ ORR), Yan et al. [20] report a Co₃O₄-O_v/N-CNTs catalyst with a remarkable H₂O₂ production rate (1.6 mol H₂O₂/(g_{cat}·h) at 0.0 V_{RHE}), the activity is attributed to the oxygen vacancies which can promote the adsorption of oxygen and optimize the OOH* binding energy. Li et al. [21] report an amorphous NiO nanosheets catalyst (a-NiO NSs), and demonstrate the correlations between Ni d-orbital states and catalytic activity. Nevertheless, these works focus on the modification of the metal oxide itself, and synergistic effects between multiple metal oxide components are rarely further studied. On the other hand, most researchers pay attention to adjusting adsorption capacity of O₂ and OOH*, ignoring the process of intermediate generation (in the alkaline solution) which take place by the following process: O₂ + H₂O + e⁻ → OOH* + OH⁻. According to the equation, the formation of OOH intermediate not only depends on the O₂ adsorption, but also is influenced by the dissociation of H₂O (as a H source) [22–24].

Herein, we report a m-Bi₂O₃/Ta₂O₅ electrocatalyst through a one-step grinding method. m-Bi₂O₃/Ta₂O₅ shows high selectivity towards 2e⁻ ORR in alkaline solution (about 94.7% at 0.4 V_{RHE}) and behaves an outstanding H₂O₂ yield (471 mmol/(g_{cat}·h)) with 91.8% FE, indicating m-Bi₂O₃/Ta₂O₅ catalyst has comparable performance to the most of reported catalysts [25–30]. The H₂O₂ solution produced at 90 min accumulation shows 100% disinfection efficacy of *P. aeruginosa*, *S. aureus* and *E. coli*. Under the guidance of both in-situ Raman and DFT, we reveal the synergistic effects between Bi₂O₃ and Ta₂O₅ in boosting 2e⁻ ORR performance, the outstanding oxygen adsorption capacity of Bi₂O₃ and the advantage of Ta₂O₅ in dissociating water contribute to a more efficient OOH* forming process and finally result in high selectivity towards H₂O₂ production. This study offers a new direction in designing more selective electrocatalysts for efficient 2e⁻ ORR.

2. Experimental section

2.1. Chemicals

Tantalum oxide (Ta₂O₅, Aladdin, 99.99%), Bismuth oxide (Bi₂O₃, Macklin, 99.999%), Potassium hydroxide (KOH, Macklin, 99.5%), Sulfuric acid (H₂SO₄, Lingfeng Chemical Reagent Co., Ltd, 99.9%), Cerium sulfate (Ce(SO₄)₂, Aladdin, 98%), Potassium titanyl oxalate (C₄K₂O₉·2H₂O, Macklin, 99%), potassium ferricyanide (K₃FeC₆N₆, Macklin, ≥99.5%), perchloric acid (HClO₄, Sinopharm Chemical Reagent Co., Ltd, 70.0 ~ 72.0%), Phosphoric acid (H₃PO₄, Macklin, ≥85 wt % in H₂O), Nafion solution (DuPont), Ethanol (CH₃OH, Sinopharm Chemical Reagent Co., Ltd, 99.5%), O₂ (99.999%) and N₂ (99.99%) were purchased from Hangzhou Jingong Special Gas Co., Ltd. All of the reagents were used without further purification.

2.2. Bacterial strains

Model bacteria selected are Gram-negative *Pseudomonas aeruginosa* (*P. aeruginosa*) Boston 41501 (ATCC27853) and *Escherichia coli* (*E. coli*) FDA strain Seattle 1946 (ATCC25922), and Gram-positive *Staphylococcus aureus* (*S. aureus*) FAD209 (ATCC6538) in this study. All bacterial strains were routinely sustained in TSB medium with 25% glycerol at –80 °C.

2.3. Preparation of m-Bi₂O₃/Ta₂O₅ catalysts

Take 10-Bi₂O₃/Ta₂O₅ as an example. After weighing 200 mg of tantalum oxide, 22.3 mg of bismuth oxide was accurately weighed according to the ten percent mass fraction of bismuth element in tantalum oxide. Transferring the powder to a mortar, adding a little ethanol for better contact, then powder was ground for about twenty minutes until all the ethanol has evaporated, powder left in the mortar was named 10-Bi₂O₃/Ta₂O₅.

2.4. Characterizations

The morphology of samples was observed through a field emission scanning electron microscope (FE-SEM, HITACHI Regulus 8100) at an acceleration voltage of 15 kV. To further observe the sub-microstructure of the catalyst, transmission electron microscope (TEM, Tecnai G2 F30 S-Twin) at 300 kV was applied, and related elemental distribution was analyzed with energy dispersive X-ray spectroscopy (EDS, Xplore 80). Zeta potential was tested in ethanol solution through Malvern Zetasizer Nano ZS90. X-ray diffraction (XRD) was performed on an X-ray diffractometer (PANalytical X-pert Pro) with Cu Kα irradiation (λ = 1.5418 Å) at 40 kV and 40 mA. The X-ray photoelectron spectroscopy (XPS) was tested by X-ray photoelectron spectroscopy (Thermo Scientific K-Alpha). In-situ Raman spectrum were characterized by the confocal Raman imaging microscope (Renishaw InVia, 532 nm laser) under different potentials (0.0–0.9 V_{RHE}) with a Ivium-n-Stat electrochemical workstation.

3. Results and discussion

3.1. Morphology and structure

m-Bi₂O₃/Ta₂O₅ was synthesized by a one-step grinding process, scanning electron microscope (SEM) and transmission electron microscope (TEM) were applied to characterize the morphology information of m-Bi₂O₃/Ta₂O₅ catalyst. The SEM images of commercial Bi₂O₃, Ta₂O₅ and 10-Bi₂O₃/Ta₂O₅ are illustrated in Fig. S1a–c. The commercial Bi₂O₃ seems to be a sheet-like structure, and the commercial Ta₂O₅ is more like a stack of spheres. It is interesting to find that the appearance of 10-Bi₂O₃/Ta₂O₅ gets an obvious change due to grinding, the surface of 10-Bi₂O₃/Ta₂O₅ becomes smooth with regular plane. TEM and HRTEM were employed to further observe the sub-microstructure of the catalyst. TEM image of 10-Bi₂O₃/Ta₂O₅ is shown in Fig. 1a, the images of Ta₂O₅ and Bi₂O₃ are presented in Fig. S2a, b. The TEM images exhibit similar geometry to SEM. Analysis of elemental species were tested by Energy Dispersive Spectrometer (Fig. S3), in addition to Cu substrates, only Ta, Bi, O three elements were detected. Focus on the HRTEM images of 10-Bi₂O₃/Ta₂O₅ (Fig. 1b, c), clear lattice fringes about 0.388 nm, 0.346 nm and 0.325 nm in length can be found (details are shown in Fig. S4a–c), which belong to Ta₂O₅ (001), Bi₂O₃ (002) and Bi₂O₃ (–121), respectively. Mapping images of 10-Bi₂O₃/Ta₂O₅ reveal that the two oxides are homogeneously mixed after grinding (Fig. 1d), which is beneficial for a further interaction between Ta₂O₅ and Bi₂O₃. Besides, Ta₂O₅ and Bi₂O₃ were dispersed in ethanol, and the zeta potential of each component was tested. The test results indicate that the different charges on the surface of the particles (Ta₂O₅ owns negative charges while Bi₂O₃ owns positive charges as shown in Fig. S4d, e) drive the two oxides integrating closer [31], which results in the uniform distribution of elements shown in mapping images.

X-Ray Diffraction (XRD) was used to characterize the crystal structure of the catalysts. As shown in Fig. 1e, commercial Ta₂O₅, Bi₂O₃ and 10-Bi₂O₃/Ta₂O₅ are taken for comparison. The diffraction peaks at 2θ = 22.8°, 28.3°, 36.6° and 55.5° are identified and indexed to (001), (1110), (1111) and (1112) crystal facets of Ta₂O₅ (PDF # No. 71–0639; Space group C2mm), respectively. The faint peaks at 25.7° and 27.4° are attributed to the (002) and (–121) crystal facet of Bi₂O₃ (PDF # No. 71–2274; Space group P21/c). The intensity of the diffraction peak is relatively weak, which is caused by the low content of Bi₂O₃ [32]. It is worth noting that the XRD result for 10-Bi₂O₃/Ta₂O₅ is close to a simple superposition of Ta₂O₅ and Bi₂O₃, and no other diffraction peak of the new phase can be found, indicating that Ta₂O₅ and Bi₂O₃ are only physically mixed without chemical bond.

Next, X-ray Photoelectron Spectroscopy (XPS) was used to explore if the chemical environment on the surface of Ta₂O₅ and Bi₂O₃ has changed. As illustrated in Fig. 2a, XPS survey shows that the spectrum of 10-Bi₂O₃/Ta₂O₅ is consist of several peaks belong to Ta₂O₅ and Bi₂O₃.

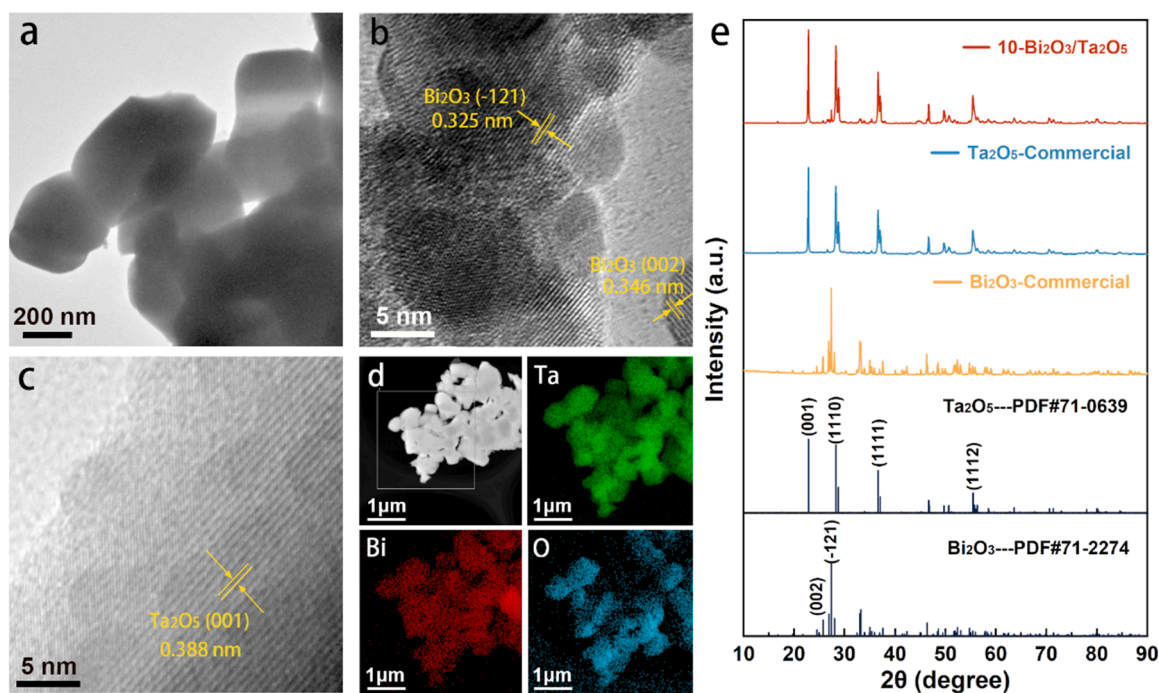


Fig. 1. (a) The TEM and (b)(c) HRTEM images of 10-Bi₂O₃/Ta₂O₅ catalyst. (d) The mapping images of 10-Bi₂O₃/Ta₂O₅ catalyst. (e) The XRD patterns of commercial Bi₂O₃, commercial Ta₂O₅ and 10-Bi₂O₃/Ta₂O₅.

The Ta 4f XPS spectrum is shown in Fig. 2b, main peaks at 26.2 eV and 28.1 eV are indexed to the Ta 4f_{7/2} and Ta 4f_{5/2}, consistent with many reports [33,34]. Note that there is no significant shift of both peaks after mixing, indicating the chemical state of the Ta remains almost unchanged by the addition of Bi₂O₃. The similar results can be observed according to the Bi 4f (Fig. 2c), both 10-Bi₂O₃/Ta₂O₅ and commercial Bi₂O₃ show two strong peaks at 158.7 eV and 164.0 eV, which belong to Bi 4f_{7/2} and Bi 4f_{5/2}, respectively [35,36]. Finally, focus on the O 1s XPS spectra of Ta₂O₅, Bi₂O₃ and 10-Bi₂O₃/Ta₂O₅ in Fig. 2d, two O species were detected. The peak at 532.1 eV can be found in commercial Ta₂O₅ and the mixture, which is belong to the adsorbed oxygen (O_A), the peak at 530.1 eV is attributed to lattice oxygen (O_L) of “Ta-O” [37]. The O_A and O_L peaks of Bi₂O₃ occur at 531.2 eV and 529.5 eV, respectively [38]. And it worth noting that the peaks at 531.2 eV and 529.5 eV disappear in the 10-Bi₂O₃/Ta₂O₅ O 1s spectra, which is caused by the low mass content of Bi₂O₃. Overall, there is no significant peak shift between the mixture and single component, suggesting the chemical states are near changeless. In addition, it is surprisingly to find the difference of O 1s XPS spectra between Ta₂O₅ and Bi₂O₃ (Fig. S5). Obviously, much oxygen adsorbed on the surface of Bi₂O₃ which results in a larger proportion of O_A (38%), about 12% higher than the Ta₂O₅ (26%). With the introduction of Bi₂O₃, the O_A content of 10-Bi₂O₃/Ta₂O₅ get a 2% slight increase than commercial Ta₂O₅. Enrichment of more oxygen on catalyst surface may be an important factor for the enhanced performance of the m-Bi₂O₃/Ta₂O₅ catalyst [39–43].

3.2. Electrocatalytic 2e⁻ ORR performance of catalysts

From the analysis of XRD and XPS test results, the introduction of Bi₂O₃ helps for a better O₂ adsorption than single commercial Ta₂O₅. To investigate the effects of Bi₂O₃ content on electrocatalytic performance, a rotating ring-disk electrode (RRDE) was used to evaluate the selectivity and activity of as-prepared catalyst towards 2e⁻ ORR. During this work, all electrochemical performances were tested in 0.1 M KOH solution. Drop-cast electrode, platinum wire and saturated calomel electrode (Hg/Hg₂Cl₂) were used as the working electrode, counter electrode and reference electrode, respectively. H₂O₂ was produced in

the glassy carbon area of the electrode, then it was transferred to the platinum ring at 1600 rpm and oxidized at 1.3 V_{RHE} ring voltage. Under such ring voltage, the water oxidation was prevented, and the change of ring current was only caused by the decomposition of the H₂O₂. The ring and disk current information was then transferred into the corresponding reaction selectivity and electron transfer numbers. As shown in Fig. 3a, cyclic voltammetry (CV) curves of 10-Bi₂O₃/Ta₂O₅ were recorded under O₂-saturated and N₂-saturated KOH solutions. Compared to the N₂ atmosphere, a strong reduction peak appears when electrolyte is saturated with O₂, indicating that the certain ORR takes place over the electrocatalyst.

The linear sweep voltammetry (LSV) curves of m-Bi₂O₃-Ta₂O₅ catalysts are shown in Fig. 3b, it is worth mentioning that ring current density of m-Bi₂O₃/Ta₂O₅ is higher than both commercial Bi₂O₃ and Ta₂O₅, implying more H₂O₂ is formed at same test conditions. Then, the H₂O₂ selectivity and electron transfer number was calculated by Equation (1) and Equation (2) (details are shown in supporting information), respectively. Selectivity and electron transfer number at 0.4 V_{RHE} are chosen as comparators, all m-Bi₂O₃/Ta₂O₅ catalysts present higher H₂O₂ selectivity and lower electron transfer number than commercial Bi₂O₃ and Ta₂O₅ as shown in Fig. 3c. It can be noted that the H₂O₂ selectivity of m-Bi₂O₃/Ta₂O₅ exhibits a “volcanic curve” with Bi content increasing, especially when Bi content was 10 wt%, 10-Bi₂O₃/Ta₂O₅ get the best 2e⁻ ORR performance among the as-prepared catalyst with a high H₂O₂ selectivity of 94.7%, which has a comparable selectivity to other metal oxide electrocatalysts shown in Table S1. The selectivity of 10-Bi₂O₃/Ta₂O₅ remains above 90% over a wide voltage range of 0–0.6 V_{RHE} as shown in Fig. S6a, suggesting that the synergistic effect between the two components greatly boosts the 2e⁻ ORR performance. Faraday efficiency (FE) was calculated by Equation (3), which also presents a volcanic distribution (Fig. 3d), FE of 10-Bi₂O₃/Ta₂O₅ reaches up to 90.0%, ca. 20% higher than both commercial Bi₂O₃ and Ta₂O₅. When content of Bi continued increasing, the H₂O₂ selectivity of 10-Bi₂O₃/Ta₂O₅ get closer to the commercial Bi₂O₃ (Fig. S6d), especially when Bi content was 50 wt%, the selectivity is as low as 85.5%, just 3.8% higher than the commercial Bi₂O₃. Tafel slope related to kinetic processes, which was obtained according to the polarization curves.

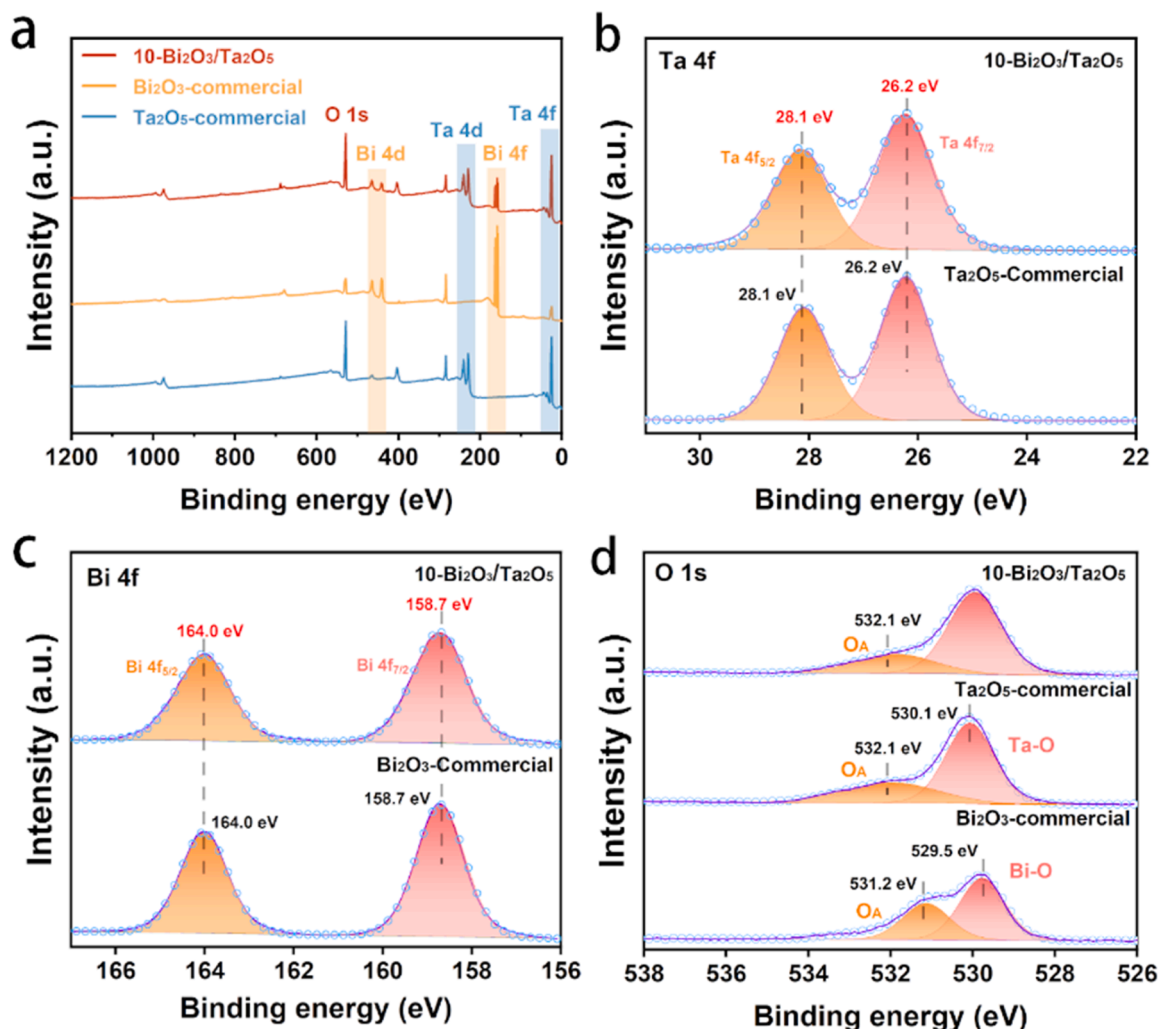


Fig. 2. (a) XPS survey of Bi_2O_3 -commercial, Ta_2O_5 -commercial and $10\text{-Bi}_2\text{O}_3/\text{Ta}_2\text{O}_5$. The comparison between $10\text{-Bi}_2\text{O}_3/\text{Ta}_2\text{O}_5$ and commercial Bi_2O_3 or Ta_2O_5 in (b) Ta 4f, (c) Bi 4f and (d) O 1s spectra.

Tafel slope of Ta_2O_5 , $5\text{-Bi}_2\text{O}_3/\text{Ta}_2\text{O}_5$, $10\text{-Bi}_2\text{O}_3/\text{Ta}_2\text{O}_5$, $15\text{-Bi}_2\text{O}_3/\text{Ta}_2\text{O}_5$, $20\text{-Bi}_2\text{O}_3/\text{Ta}_2\text{O}_5$, Bi_2O_3 was 114.3 mV/dec, 63.1 mV/dec, 54.3 mV/dec, 62.7 mV/dec, 85.9 mV/dec, 110.6 mV/dec, respectively (Fig. 3e). Among them, $10\text{-Bi}_2\text{O}_3/\text{Ta}_2\text{O}_5$ has the lowest Tafel slope, indicating the fastest oxygen reduction kinetic process [44]. In order to assess the original catalytic activity, it is necessary to analyze the active surface area of catalyst which actually participating in electrochemical reactions. Electrochemical active surface area (ECSA) was measured by testing the capacitance of the double layer capacitance (C_{dl}) with CV curves. Potential was controlled within $0.85 V_{\text{RHE}}$ and $1.15 V_{\text{RHE}}$ to avoid the redox reactions, CV curves at different scan rates are presented in Fig. S7. The $10\text{-Bi}_2\text{O}_3/\text{Ta}_2\text{O}_5$ catalyst owns the highest ECSA ($0.67 \text{ mF}/\text{cm}^2$, Fig. S8), suggesting more active sites for ORR. Electrochemical impedance spectroscopy (EIS) was carried out on CHI761E electrochemical workstation with a three-electrode system (Fig. S9). Obviously, $10\text{-Bi}_2\text{O}_3/\text{Ta}_2\text{O}_5$ exhibits the smallest diameter of impedance arc (DIA), revealing the most efficient charge transfer process [45–47]. Finally, an 80-hour stability test of $10\text{-Bi}_2\text{O}_3/\text{Ta}_2\text{O}_5$ was tested in a O_2 -saturated 0.1 M KOH solution (Fig. 3f), setting E_{Disk} at $0.4 V_{\text{RHE}}$ and O_2 flow rate was controlled at $15 \text{ mL}/\text{min}$. Current fluctuated within a small range during stability test, and no significant shift occurred between LSV and CV curves (Fig. S10) curves before and after the test, meaning $10\text{-Bi}_2\text{O}_3/\text{Ta}_2\text{O}_5$ has an excellent stability.

3.3. Electrocatalytic mechanism

In order to have a deeper understanding of the reaction mechanism, in-situ Raman spectroscopy measurements got applied to detect the intermediates formed on the catalyst surface during the reaction (devices placement are shown in Fig. S11). The catalyst powder was distributed into an ethanol solution and then coated over a $2 \text{ cm} \times 2 \text{ cm}$ carbon cloth, after drying, the carbon cloth was loaded in the in-situ Raman cell. The in-situ Raman was tested under N_2 -saturated or O_2 -saturated atmosphere, during the test process, voltage varied between 0.0 and $0.9 V_{\text{RHE}}$ according to a pre-set procedure. For a better observation of peak changes between different conditions, a 0.1 M KOH added with 50 mmol KClO_4 was used as the electrolyte, and the peak of ClO_4^- was taken as the reference. To reduce testing errors, exposure time was set to three seconds as well as a twenty-times results accumulation. First, the commercial Bi_2O_3 was tested in a N_2 -saturated electrolyte, according to the results as illustrated in Fig. 4a, the vibration peak located at 933 cm^{-1} is assigned to ClO_4^- [48], apart from the main peaks belong to Bi_2O_3 ($0\text{--}500 \text{ cm}^{-1}$) and carbon ($1300\text{--}1600 \text{ cm}^{-1}$), there exists no other.

peak. When the electrolyte was saturated with O_2 (shown in Fig. 4b), the peak at 1060 cm^{-1} appeared, therefore, it was regarded as the O_2^* species [49]. However, there were no other obvious peaks within the wave number range of $700\text{--}1200 \text{ cm}^{-1}$, indicating only trace amounts of “OOH” and “OH” intermediate species were formed during the reaction.

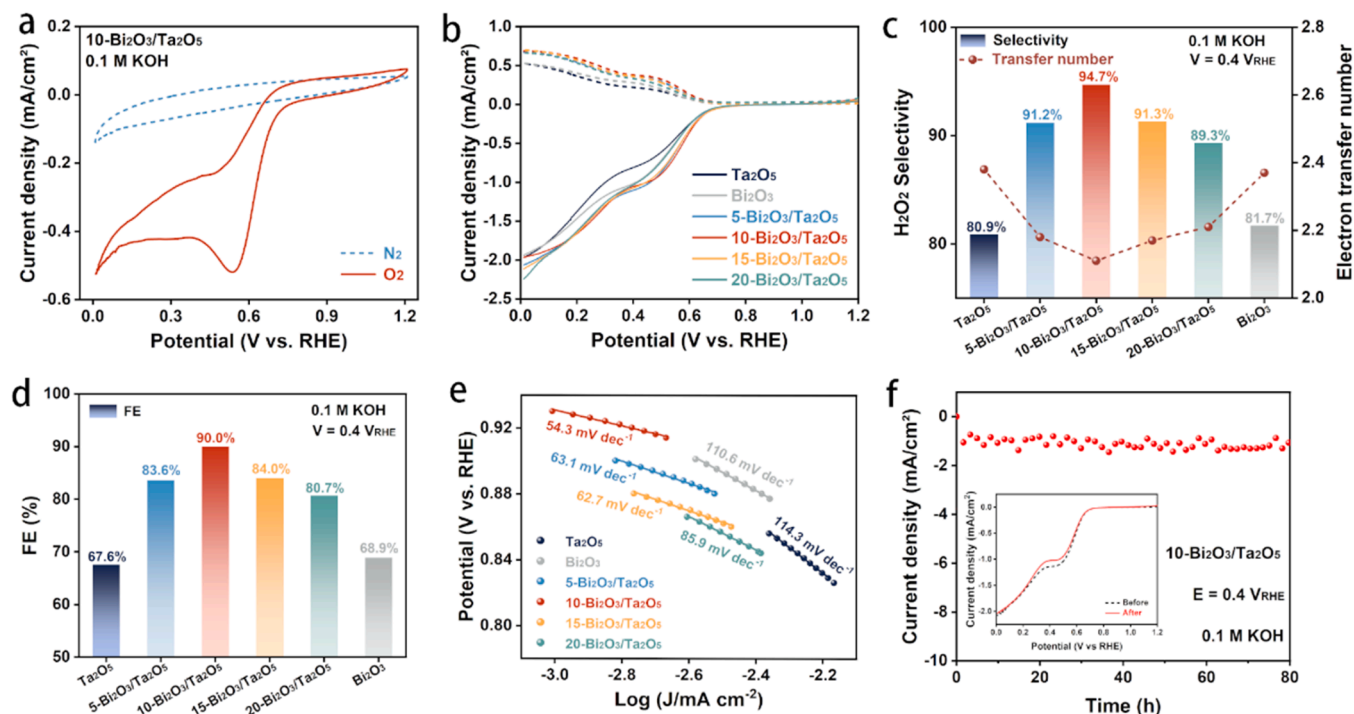


Fig. 3. Electrochemical performance of m-Bi₂O₃/Ta₂O₅ catalyst. (a) CV curves of 10-Bi₂O₃/Ta₂O₅ test in O₂ (red line) /N₂ (blue line) - saturated electrolyte. (b) LSV curves about catalysts with different bismuth mass content. (c) H₂O₂ selectivity, electron transfer number and (d) Faraday efficiency at 0.4 V_{RHE}. (e) Tafel slopes of m-Bi₂O₃/Ta₂O₅ catalyst. (f) 80 h electrochemical stability test of 10-Bi₂O₃/Ta₂O₅ catalyst, the inset represents the LSV curves of 10-Bi₂O₃/Ta₂O₅ measured before and after test.

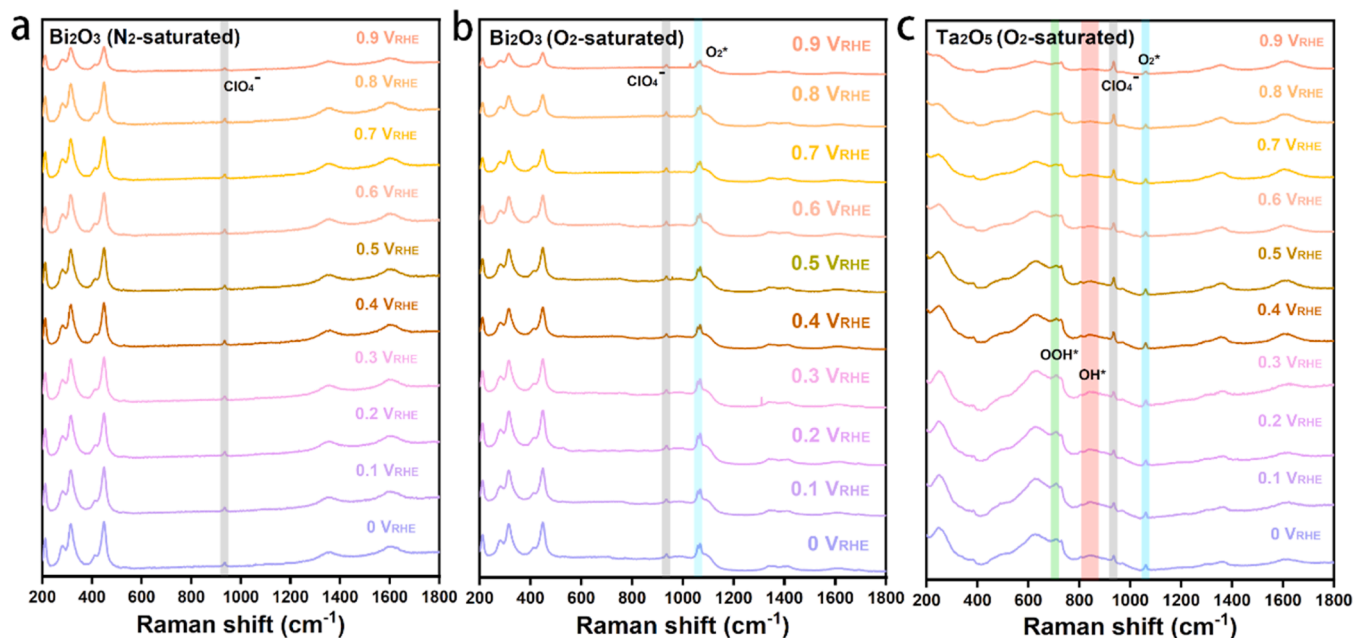


Fig. 4. In-situ Raman spectra results of (a) Bi₂O₃ (tested in N₂-saturated electrolyte) (b) Bi₂O₃ (tested in O₂-saturated electrolyte) and (c) Ta₂O₅ (tested in O₂-saturated electrolyte) at various applied potentials (vs RHE).

The results of Ta₂O₅ tested in O₂-saturated electrolyte were shown in Fig. 4c, comparing to the Bi₂O₃, it is obvious that the O₂^{*} signal peak becomes much weaker relative to the peak of ClO₄⁻. When the voltage gradually becomes negative, it could be observed that a peak occurs at about 720 cm⁻¹, which is caused by the accumulation of the OOH^{*}-species [50,51]. Within the 800–900 cm⁻¹ Raman shift, broad peaks gradually appear under 0.6 V_{RHE} and more negative voltages. In spite of

the original peak of Ta₂O₅, such changes can be attributed to the formation of OH^{*} [52]. In summary, based on the in-situ Raman results of Bi₂O₃, such strong O₂^{*} signal peak suggests that Bi₂O₃ possesses an excellent O₂ adsorption capacity which is consistent with the O 1s spectrum results as mentioned before. The difficulty in detecting OH^{*} and OOH^{*} indicates that Bi₂O₃ has a poor ability to dissociate H₂O which results in the lack of “H” to form OOH intermediates. On the

contrary, in the Raman spectra of Ta_2O_5 , peaks belong to OH^* suggest that the H_2O dissociation takes place much efficient over Ta_2O_5 than Bi_2O_3 , and the weak O_2^* peak implies that the lack of O_2 is the limiting factor for efficient 2e^- ORR on Ta_2O_5 . Here in, it can be inferred that Ta_2O_5 and Bi_2O_3 each play a role in the 2e^- ORR process: the superior O_2 adsorption capacity of Bi_2O_3 guarantees the supply of O_2 , and the Ta_2O_5 can dissociate the H_2O to provide plenty of H. When combining the Bi_2O_3 and Ta_2O_5 together, the synergistic effects between two components can finally boost the 2e^- ORR performance.

Density functional theory (DFT) was used to further clarify the 2e^- ORR mechanism over m- $\text{Bi}_2\text{O}_3/\text{Ta}_2\text{O}_5$ electrocatalyst, and all calculations of Bi_2O_3 and Ta_2O_5 were based on the stable crystal face (001). First, the O_2 adsorption structures of Ta_2O_5 and Bi_2O_3 were calculated (Fig. 5a, b). It is obvious that the O_2 molecule tends to adsorbed on Bi_2O_3 by a strong chemisorption rather than a weak physisorption on the Ta_2O_5 . The results about E_{O_2} of Bi_2O_3 is -1.97 eV, which is better than that on Ta_2O_5 ($E_{\text{O}_2} = -0.06$ eV). It is in accord with the stronger adsorbed oxygen peak on the Raman spectra of Bi_2O_3 in Fig. 4b. In addition, dissociation of H_2O ensures the supply of H to form the OOH intermediate, which plays an important role in 2e^- ORR. Then, the

adsorption energy of H_2O as well as the H and OH were calculated. Comparing the results shown in Fig. 5c-d and Figure 5e-f, H_2O tends to be adsorbed on Ta_2O_5 ($E_{\text{H}_2\text{O}} = -0.83$ eV) easier than that on Bi_2O_3 ($E_{\text{H}_2\text{O}} = -0.20$ eV). Besides, Ta_2O_5 shows a better capacity in stabilizing OH and H ($E_{\text{H}+\text{OH}} = -0.93$ eV) than Bi_2O_3 ($E_{\text{H}+\text{OH}} = -0.12$ eV), which can provide appropriate amount of H for the formation of OOH intermediate. And it is no wonder that Raman peaks of OH^* and OOH^* can only be detected on Ta_2O_5 rather than Bi_2O_3 , which was shown in Fig. 4b, c. Meanwhile, it is interesting to discover that OOH can only exist on Ta_2O_5 surfaces while it breaks into OH and O on Bi_2O_3 (Fig. 5g, h). It implies that too much Bi_2O_3 is detrimental to H_2O_2 production, which is consistent with the results shown in Fig. S6d. Above all, the excellent O_2 adsorption capacity of Bi_2O_3 ensures the supply of O_2 , and the Ta_2O_5 can dissociate the H_2O to supply numerous H. The synergistic effects between Bi_2O_3 and Ta_2O_5 result in an efficient OOH formation process, and eventually boost the 2e^- ORR selectivity.

3.4. H_2O_2 production

A H-cell was used to evaluate the H_2O_2 yield (Fig. 6a), the methods for calculating H_2O_2 yield and FE have detailed descriptions in the [Supplementary Information](#). A Ir-Ta-Ti sheet was used as the anode electrode of H-cell, cathode electrode was a gas diffusion layer (GDL) carbon paper with catalyst powder (4 mg/cm^2). All H_2O_2 yield tests were in a 0.1 M KOH solution, and the only O_2 channel was setting under the cathode electrode to enhance the contact between oxygen and catalyst with the opposite flow. In order to found an optimum condition to produce H_2O_2 , the effects of current on H_2O_2 yield and FE were firstly examined. As illustrated in Fig. 6b, under different currents from 50 to 130 mA, the H_2O_2 yield reached the highest at 110 mA, about $471 \text{ mmol H}_2\text{O}_2$ was produced per gram catalyst each hour with 91.8% FE. The H_2O_2 yield decreases to $443 \text{ mmol}/(\text{g}_{\text{cat}}\cdot\text{h})$ when increasing current to 130 mA, and the FE suddenly falls down to 73.1%. For the consideration of both H_2O_2 yield and FE, 110 mA current was selected as the optimum current condition. The distribution of H_2O_2 yield test over different catalysts are very similar to the H_2O_2 selectivity test results, which also show a volcanic curve. The commercial Ta_2O_5 and Bi_2O_3 behaves.

an insufficient H_2O_2 production capacity (364 and $368 \text{ mmol}/(\text{g}_{\text{cat}}\cdot\text{h})$, respectively) due to their low H_2O_2 selectivity, the m- $\text{Bi}_2\text{O}_3/\text{Ta}_2\text{O}_5$ produce more H_2O_2 with same test conditions, $400 \text{ mmol}/(\text{g}_{\text{cat}}\cdot\text{h})$ of 5- $\text{Bi}_2\text{O}_3/\text{Ta}_2\text{O}_5$, $471 \text{ mmol}/(\text{g}_{\text{cat}}\cdot\text{h})$ of 10- $\text{Bi}_2\text{O}_3/\text{Ta}_2\text{O}_5$, $419 \text{ mmol}/(\text{g}_{\text{cat}}\cdot\text{h})$ of 15- $\text{Bi}_2\text{O}_3/\text{Ta}_2\text{O}_5$ and $379 \text{ mmol}/(\text{g}_{\text{cat}}\cdot\text{h})$ of 20- $\text{Bi}_2\text{O}_3/\text{Ta}_2\text{O}_5$. Furthermore, a cycle experiment was examined to test the stability of catalyst in actual production- H_2O_2 yield was tested each hour under 110 mA current in 0.1 M KOH solution, the result was recorded as one cycle, and the fresh cathode electrolyte was used in the next cycle test. As shown in Fig. 6d, the H_2O_2 yield is always at a high value about $465 \text{ mmol}/(\text{g}_{\text{cat}}\cdot\text{h})$, and the FE maintains near 90%, fluctuates within a very small range. The results of cycle test indicates that the 10- $\text{Bi}_2\text{O}_3/\text{Ta}_2\text{O}_5$ catalyst keeps a steady activity towards 2e^- ORR. Finally, the catalyst was continually tested in H-cell for 18 h, and the H_2O_2 concentration accumulated to 6044 ppm as shown in Fig. S13.

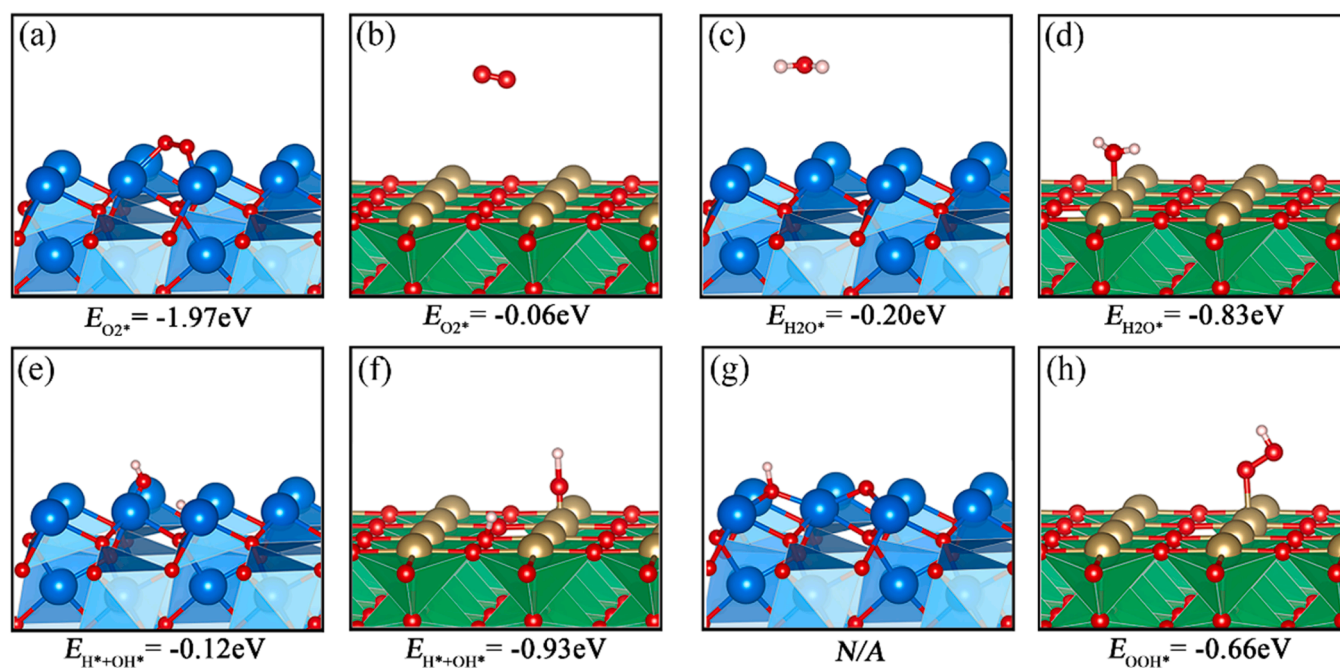


Fig. 5. Optimized structures of the intermediate states of 2e^- ORR and the related H_2O dissociation reactions: (a)(b) O_2 adsorption, (c)(d) H_2O adsorption and (e)(f) H_2O dissociation and (g)(h) OOH adsorption structures as well as the adsorption energy for different intermediate structures and H_2O dissociation reactions on Bi_2O_3 (001) and Ta_2O_5 (001). Blue spheres are Bi, red spheres are O, white spheres are H and brown spheres are Ta.

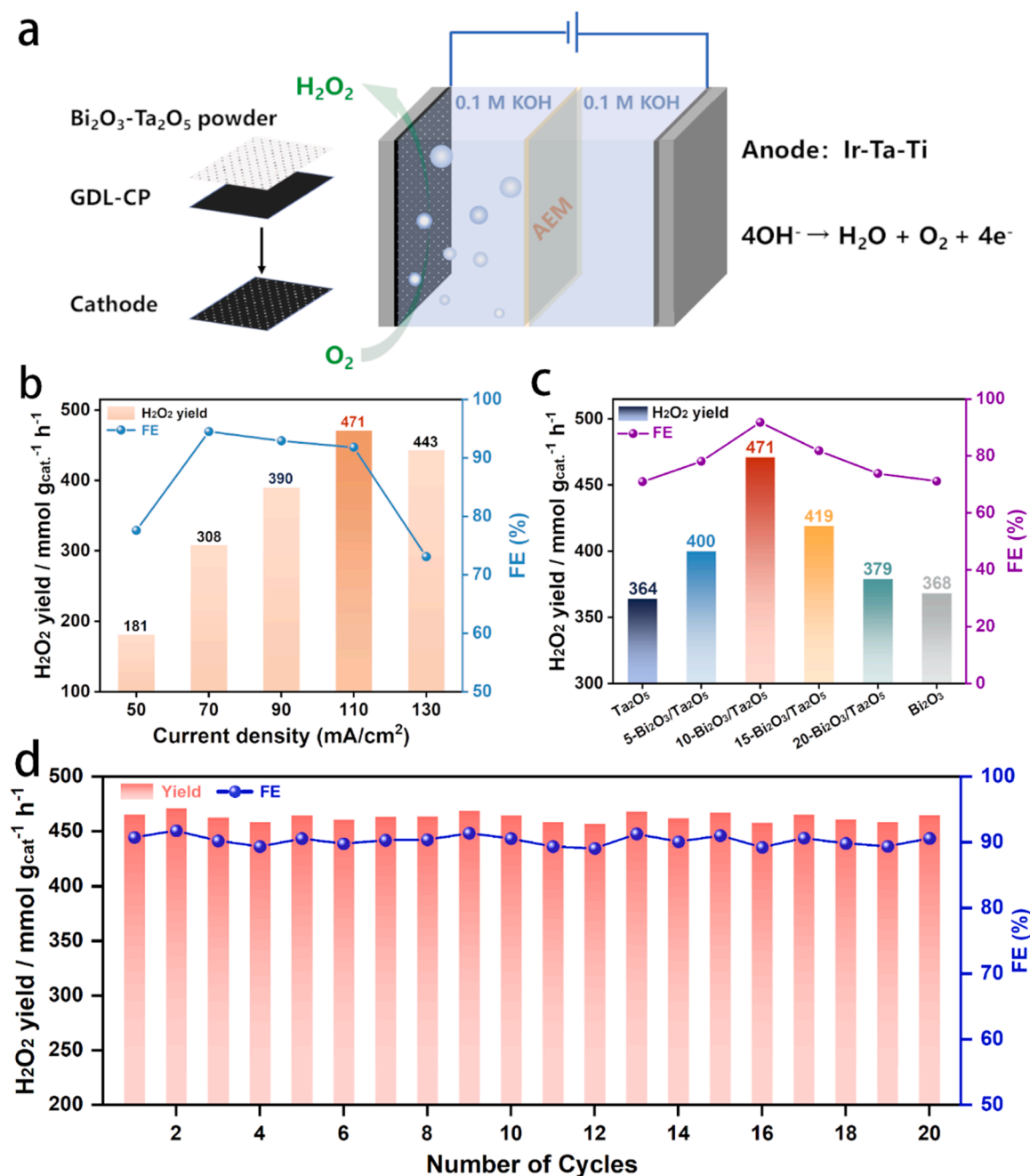


Fig. 6. (a) Diagram of the H-cell device. (b) Plot of H₂O₂ yield against current density. (c) H₂O₂ yield of commercial Ta₂O₅, Bi₂O₃ and m-Bi₂O₃/Ta₂O₅ electrocatalyst. (d) Cycle tests of 10-Bi₂O₃/Ta₂O₅ under 110 mA current.

3.5. Disinfection experiments via on-site production of H₂O₂

Moreover, disinfection of the typical bacteria through on-site production of H₂O₂ was tested [53,54]. The bactericidal efficiency of different H₂O₂ concentrations on *P. aeruginosa* was shown in Fig. 7a. In the as-prepared 500 ppm H₂O₂ solution, *P. aeruginosa* inoculated was deactivated totally after 20 min. Then, to assess the capacity of H₂O₂ solution produced at different accumulation times in the H-cell for bacterial disinfection, the interval tests were conducted. As shown in Fig. 7b, the H₂O₂ solution produced at 0 min and 30 min are difficult to completely deactivate *P. aeruginosa* within 30 min, in which the amount of bacterium colony can be observed after treatment (Fig. S16-17). It worth noting that extending the reaction time for H₂O₂ production, the H₂O₂ solution produced at 60 min shows a 99% bactericidal efficiency

of *P. aeruginosa* in 30 min, the number of bacterium colony.

nearly reduces to 0 (Fig. S18). When loading the H₂O₂ solution produced at 90 min, the *P. aeruginosa* can be completely deactivated (Fig. 7 c and S19). Meanwhile, the H₂O₂ solution produced at 90 min was also used to evaluate disinfections of *E. coli* and *S. aureus*, the resulted bacterial efficiencies after 30 min are similar with that of *P. aeruginosa* (shown in Fig. 7 d, e). Overall, H-cell assembled with 10-Bi₂O₃/Ta₂O₅ electrocatalyst shows a satisfying H₂O₂ production capacity applying for water disinfection. These results imply that the electrochemical on-site production of H₂O₂ has the great potential usage in environmental applications.

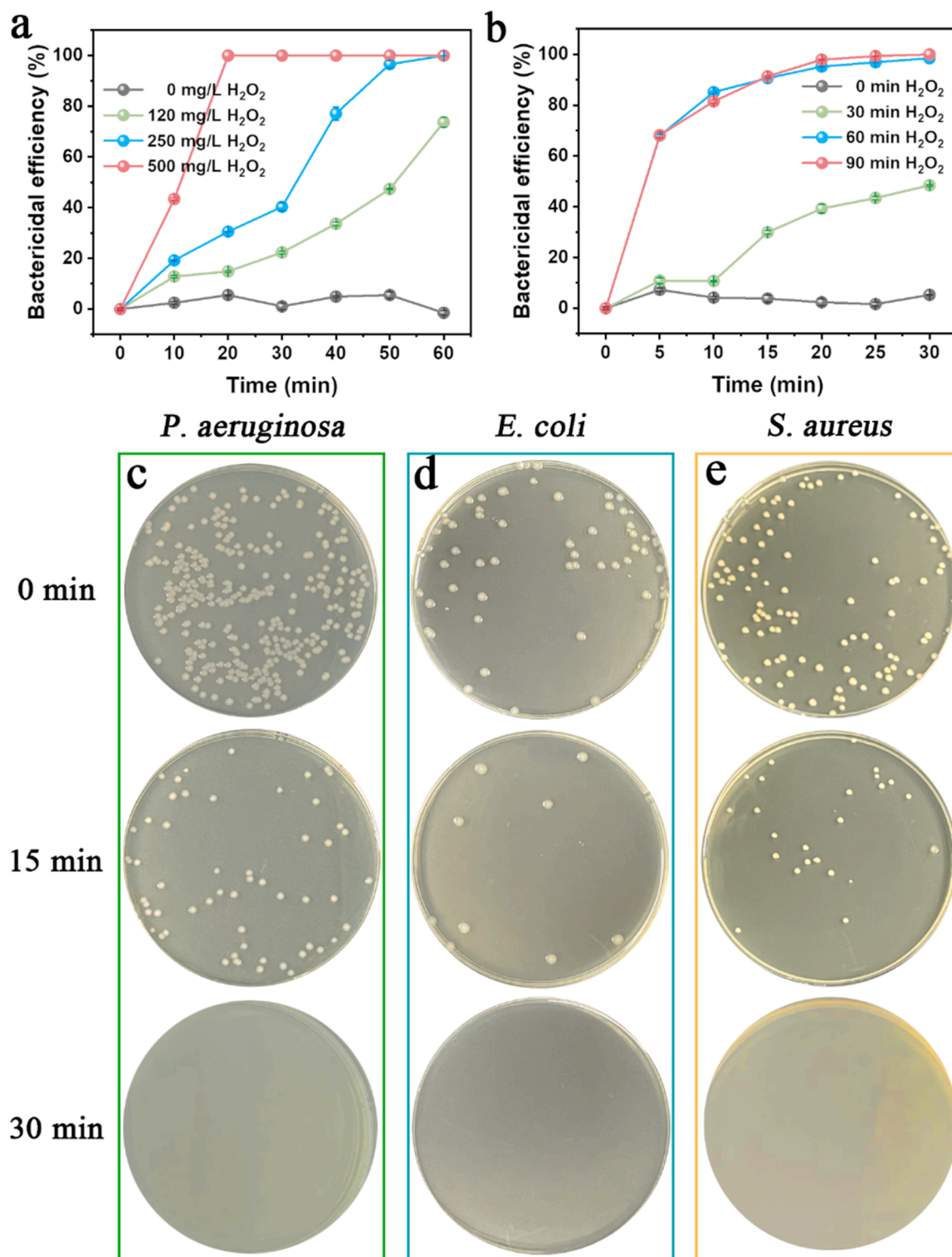


Fig. 7. Comparison of the disinfection efficacies of *P. aeruginosa* cells in (a) different concentrations H_2O_2 and (b) H_2O_2 solution produced at different accumulation times. Corresponding colony number of (c) *P. aeruginosa*, (d) *E. coli* and (e) *S. aureus* at 0, 15 and 30 min, respectively.

4. Conclusion

In summary, the m- Bi_2O_3/Ta_2O_5 electrocatalyst was fabricated through physical mixing. The 10- Bi_2O_3/Ta_2O_5 exhibits significantly enhanced $2e^-$ ORR performance in the 0.1 M KOH with 94.7% selectivity, and it also has excellent durability for 80 h at a constant potential of 0.4 V_{RHE} . While assembled 10- Bi_2O_3/Ta_2O_5 in homemade H-cell as

cathode, H_2O_2 yield reaches up to 471 mmol/(g_{cat}·h) with 91.8% FE, and remains active towards H_2O_2 production after 20 times cycle experiments. The $2e^-$ ORR mechanism over 10- Bi_2O_3/Ta_2O_5 is proposed under the guidance of in-situ Raman spectra and theoretical calculations. The superior O_2 adsorption capacity of Bi_2O_3 guarantees the supply of O_2 , and the Ta_2O_5 dissociates the H_2O to provide plenty of H. The synergistic effects of Bi_2O_3 and Ta_2O_5 contribute to an efficient

OOH* formation process over m-Bi₂O₃/Ta₂O₅ catalyst, and eventually boost the 2e⁻ ORR selectivity. Moreover, the H₂O₂ solution produced at 90 min can completely deactivate *P. aeruginosa*, *E. coli* and *S. aureus* within 30 min, implying that the strategy about on-site production of H₂O₂ applying in water disinfection is feasible. This work provides a new insight into the design of metal oxides electrocatalyst, and preliminarily explores the applications of on-site production of low-concentration H₂O₂ in water disinfection.

CRedit authorship contribution statement

Chenghang Jiang: Writing – original draft, Validation, Formal analysis, Methodology, Investigation, Conceptualization, Data curation. **Yan-Fei Fei:** Validation, Formal analysis, Methodology, Visualization, Conceptualization, Data curation. **Weiwei Xu:** Methodology, Formal analysis, Validation. **Zhikang Bao:** Resources, Methodology, Data curation. **Yizhen Shao:** Validation, Formal analysis. **Shijie Zhang:** Methodology, Writing – review & editing, Supervision, Project administration. **Zhong-Ting Hu:** Methodology, Writing – review & editing, Resources, Project administration. **Jianguo Wang:** Methodology, Writing – review & editing, Funding acquisition, Resources, Supervision, Project administration.

Declaration of Competing Interest

The authors declare that they have no known competing financial interests or personal relationships that could have appeared to influence the work reported in this paper.

Data Availability

No data was used for the research described in the article.

Acknowledgements

The authors acknowledge the financial support from the National Key Research and Development Program of China (2021YFA1500900), and the National Natural Science Foundation of China (U21A20298 and 22141001).

Appendix A. Supporting information

Supplementary data associated with this article can be found in the online version at doi:10.1016/j.apcatb.2023.122867.

References

- [1] Q. Zhao, J. An, S. Wang, Y. Qiao, C. Liao, C. Wang, X. Wang, N. Li, Superhydrophobic air-breathing cathode for efficient hydrogen peroxide generation through two-electron pathway oxygen reduction reaction, *ACS Appl. Mater. Interfaces* 11 (2019) 35410–35419.
- [2] S. Yang, A. Verdager-Casadevall, L. Arnarson, L. Silvioli, V. Čolić, R. Frydendal, J. Rossmeisl, I. Chorkendorff, I.E.L. Stephens, Toward the decentralized electrochemical production of H₂O₂: a focus on the catalysis, *ACS Catal.* 8 (2018) 4064–4081.
- [3] S. Kato, J.U. Jung, T. Suenobu, S. Fukuzumi, Production of hydrogen peroxide as a sustainable solar fuel from water and dioxygen, *Energy Environ. Sci.* 6 (2013) 3756–3764.
- [4] B.-Q. Li, C.-X. Zhao, J.-N. Liu, Q. Zhang, Electrosynthesis of hydrogen peroxide synergistically catalyzed by atomic Co–Nx–C sites and oxygen functional groups in noble-metal-free electrocatalysts, *Adv. Mater.* 31 (2019) 1808173.
- [5] J.M. Campos-Martin, G. Blanco-Brieva, J.L.G. Fierro, Hydrogen peroxide synthesis: an outlook beyond the anthraquinone, *Process, Angew. Chem. Int. Ed.* 45 (2006) 6962–6984.
- [6] R.J. Lewis, M. Koy, M. Macino, M. Das, J.H. Carter, D.J. Morgan, T.E. Davies, J. B. Ernst, S.J. Freakley, F. Glorius, G.J. Hutchings, N-Heterocyclic carbene modified palladium catalysts for the direct synthesis of hydrogen peroxide, *J. Am. Chem. Soc.* 144 (2022) 15431–15436.
- [7] X.T. Tran, V.L.N. Vo, Y.-M. Chung, Fast microwave-assisted synthesis of iron–palladium catalysts supported on graphite for the direct synthesis of H₂O₂, *Catal. Today* (2022).
- [8] A. Rodriguez-Gomez, F. Platero, A. Caballero, G. Colon, Improving the direct synthesis of hydrogen peroxide from hydrogen and oxygen over Au-Pd/SBA-15 catalysts by selective functionalization, *Mol. Catal.* 445 (2018) 142–151.
- [9] J. Kim, Y.M. Chung, S.M. Kang, C.H. Choi, B.Y. Kim, Y.T. Kwon, T.J. Kim, S.H. Oh, C.S. Lee, Palladium nanocatalysts immobilized on functionalized resin for the direct synthesis of hydrogen peroxide from hydrogen and oxygen, *ACS Catal.* 2 (2012) 1042–1048.
- [10] H. Sheng, E.D. Hermes, X. Yang, D. Ying, A.N. Janes, W. Li, J.R. Schmidt, S. Jin, Electrocatalytic production of H₂O₂ by selective oxygen reduction using earth-abundant cobalt pyrite (CoS₂), *ACS Catal.* 9 (2019) 8433–8442.
- [11] S. Chu, Y. Cui, N. Liu, The path towards sustainable energy, *Nat. Mater.* 16 (2016) 16–22.
- [12] J. Zhang, J. Ma, T.S. Choksi, D. Zhou, S. Han, Y.-F. Liao, H.B. Yang, D. Liu, Z. Zeng, W. Liu, X. Sun, T. Zhang, B. Liu, Strong metal–support interaction boosts activity, selectivity, and stability in electrosynthesis of H₂O₂, *J. Am. Chem. Soc.* 144 (2022) 2255–2263.
- [13] X. Zhao, H. Yang, J. Xu, T. Cheng, Y. Li, Bimetallic PdAu nanoframes for electrochemical H₂O₂ production in acids, *ACS Mater. Lett.* 3 (2021) 996–1002.
- [14] J. Zhang, J. Lang, Y. Wei, Q. Zheng, L. Liu, Y.-H. Hu, B. Zhou, C. Yuan, M. Long, Efficient photocatalytic H₂O₂ production from oxygen and pure water over graphitic carbon nitride decorated by oxidative red phosphorus, *Appl. Catal. B* 298 (2021), 120522.
- [15] S. Xu, R. Lu, K. Sun, J. Tang, Y. Cen, L. Luo, Z. Wang, S. Tian, X. Sun, Synergistic effects in N,O-comodified carbon nanotubes boost highly selective electrochemical oxygen reduction to H₂ O₂, *Adv. Sci.* 9 (2022), e2201421.
- [16] Y. Wu, Z. Gao, Y. Feng, Q. Cui, C. Du, C. Yu, L. Liang, W. Zhao, J. Feng, J. Sun, R. Yang, J. Sun, Harnessing selective and durable electrosynthesis of H₂O₂ over dual-defective yolk-shell carbon nanosphere toward on-site pollutant degradation, *Appl. Catal. B* 298 (2021), 120572.
- [17] Z. Bao, J. Zhao, S. Zhang, L. Ding, X. Peng, G. Wang, Z. Zhao, X. Zhong, Z. Yao, J. Wang, Synergistic effect of doped nitrogen and oxygen-containing functional groups on electrochemical synthesis of hydrogen peroxide, *J. Mater. Chem. A* 10 (2022) 4749–4757.
- [18] E.R. Hamo, B.A. Rosen, Transition metal carbides as cathode supports for PEM fuel cells, *Nano Res* (2022).
- [19] X. Peng, S. Zhang, Z. Bao, L. Ding, G. Wang, Y. Shao, Z. Xu, W. Ji, G. Feng, S. Wang, X. Zhong, J. Wang, Oxygen vacancies on Nb₂O₅ enhanced the performance of H₂O₂ electrosynthesis from O₂ reduction, *Chem. Commun.* 58 (2022) 8428–8431.
- [20] L.N. Yan, X. Cheng, Y.S. Wang, Z.Z. Wang, L.R. Zheng, Y. Yan, Y. Lu, S.R. Sun, W. G. Qiu, G. Chen, Exsolved Co₃O₄ with tunable oxygen vacancies for electrocatalytic H₂O₂ production, *Mater. Today Energy* 24 (2022).
- [21] R. Li, S. Yang, Y. Zhang, G. Yu, C. Wang, C. Chen, G. Wu, R. Sun, G. Wang, X. Zheng, W. Yan, G. Wang, D. Rao, X. Hong, Short-range order in amorphous nickel oxide nanosheets enables selective and efficient electrochemical hydrogen peroxide production, *Cell Rep. Phys. Sci.* 3 (2022), 100788.
- [22] Z. Xu, J. Liang, Y. Wang, K. Dong, X. Shi, Q. Liu, Y. Luo, T. Li, Y. Jia, A.M. Asiri, Z. Feng, Y. Wang, D. Ma, X. Sun, Enhanced electrochemical H₂O₂ production via two-electron oxygen reduction enabled by surface-derived amorphous oxygen-deficient TiO_{2-x}, *ACS Appl. Mater. Interfaces* 13 (2021) 33182–33187.
- [23] K. Dong, J. Liang, Y. Wang, L. Zhang, Z. Xu, S. Sun, Y. Luo, T. Li, Q. Liu, N. Li, B. Tang, A.A. Alshehri, Q. Li, D. Ma, X. Sun, Conductive two-dimensional magnesium metal–organic frameworks for high-efficiency O₂ electroreduction to H₂O₂, *ACS Catal.* 12 (2022) 6092–6099.
- [24] K. Dong, J. Liang, Y. Wang, Z. Xu, Q. Liu, Y. Luo, T. Li, L. Li, X. Shi, A.M. Asiri, Q. Li, D. Ma, X. Sun, Honeycomb carbon nanofibers: a superhydrophilic O₂-entrapping electrocatalyst enables ultrahigh mass activity for the two-electron oxygen reduction reaction, *Angew. Chem. Int. Ed.* 60 (2021) 10583–10587.
- [25] H. Gong, Z. Wei, Z. Gong, J. Liu, G. Ye, M. Yan, J. Dong, C. Allen, J. Liu, K. Huang, R. Liu, G. He, S. Zhao, H. Fei, Low-coordinated Co–N–C on oxygenated graphene for efficient electrocatalytic H₂O₂ production, *Adv. Funct. Mater.* 32 (2022), 2106886.
- [26] C. Xiao, L. Cheng, Y. Zhu, G. Wang, L. Chen, Y. Wang, R. Chen, Y. Li, C. Li, Super-coordinated nickel N₄Ni₁O₂ site single-atom catalyst for selective H₂O₂ electrosynthesis at high current densities, *Angew. Chem. Int. Ed.* 61 (e202206544) (2022).
- [27] P. Zhang, Y. Tong, Y. Liu, J.J.M. Vequizo, H. Sun, C. Yang, A. Yamakata, F. Fan, W. Lin, X. Wang, W. Choi, Heteroatom dopants promote two-electron O₂ reduction for photocatalytic production of H₂O₂ on polymeric carbon nitride, *Angew. Chem. Int. Ed.* 59 (2020) 16209–16217.
- [28] P. Su, M. Zhou, X. Lu, W. Yang, G. Ren, J. Cai, Electrochemical catalytic mechanism of N-doped graphene for enhanced H₂O₂ yield and in-situ degradation of organic pollutant, *Appl. Catal. B* 245 (2019) 583–595.
- [29] Z. Xu, Y. Li, Y. Cao, R. Du, Z. Bao, S. Zhang, F. Shao, W. Ji, J. Yang, G. Zhuang, S. Deng, Z. Wei, Z. Yao, X. Zhong, J. Wang, Trace water triggers high-efficiency photocatalytic hydrogen peroxide production, *J. Energy Chem.* 64 (2022) 47–54.
- [30] H. Shen, N. Qiu, L. Yang, X. Guo, K. Zhang, T. Thomas, S. Du, Q. Zheng, J. P. Attfield, Y. Zhu, M. Yang, Boosting oxygen reduction for high-efficiency H₂O₂ electrosynthesis on oxygen-coordinated Co–N–C catalysts, *Small* 18 (2022) 2200730.
- [31] Z. Xu, S. Gong, W. Ji, S. Zhang, Z. Bao, Z. Zhao, Z. Wei, X. Zhong, Z.-T. Hu, J. Wang, Photocatalysis coupling hydrogen peroxide synthesis and in-situ radical transform for tetracycline degradation, *Chem. Eng. J.* 446 (2022), 137009.
- [32] F. Yang, S.P. Ding, H.B. Song, N. Yan, Single-atom Pd dispersed on nanoscale anatase TiO₂ for the selective hydrogenation of phenylacetylene, *Sci. China Mater.* 63 (2020) 982–992.

- [33] R. Nashed, P. Szymanski, M.A. El-Sayed, N.K. Allam, Self-assembled nanostructured photoanodes with staggered bandgap for efficient solar energy conversion, *ACS Nano* 8 (2014) 4915–4923.
- [34] X. Yu, W. Li, Z.H. Li, J.W. Liu, P.A. Hu, Defect engineered Ta₂O₅ nanorod: one-pot synthesis, visible-light driven hydrogen generation and mechanism, *Appl. Catal. B* 217 (2017) 48–56.
- [35] S.J. Yang, Y.J. Ping, L.B. Qian, J.Z. Han, B.Y. Xiong, J.J. Li, P.F. Fang, C.Q. He, Flower-like Bi₂O₃ with enhanced rate capability and cycling stability for supercapacitors, *J. Mater. Sci.* 31 (2020) 2221–2230.
- [36] S. Ansari, M.S. Ansari, S.P. Satsangee, R. Jain, Bi₂O₃/ZnO nanocomposite: Synthesis, characterizations and its application in electrochemical detection of balofloxacin as an anti-biotic drug, *J. Pharm. Anal.* 11 (2021) 57–67.
- [37] X. Yu, Z.H. Li, J.W. Liu, P.G. Hu, Ta-O-C chemical bond enhancing charge separation between Ta⁴⁺ doped Ta₂O₅ quantum dots and cotton-like g-C₃N₄, *Appl. Catal. B* 205 (2017) 271–280.
- [38] J. Zhang, Y. Lu, L. Ge, C. Han, Y. Li, Y. Gao, S. Li, H. Xu, Novel AuPd bimetallic alloy decorated 2D BiVO₄ nanosheets with enhanced photocatalytic performance under visible light irradiation, *Appl. Catal. B* 204 (2017) 385–393.
- [39] H. Zhang, Y. Li, Y. Zhao, G. Li, F. Zhang, Carbon black oxidized by air calcination for enhanced H₂O₂ generation and effective organics degradation, *ACS Appl. Mater. Interfaces* 11 (2019) 27846–27853.
- [40] W. Zhou, L. Xie, J. Gao, R. Nazari, H. Zhao, X. Meng, F. Sun, G. Zhao, J. Ma, Selective H₂O₂ electrosynthesis by O-doped and transition-metal-O-doped carbon cathodes via O₂ electroreduction: a critical review, *Chem. Eng. J.* 410 (2021), 128368.
- [41] K.H. Koh, A.H. Bagherzadeh Mostaghimi, Q. Chang, Y.J. Kim, S. Siahrostami, T. H. Han, Z. Chen, Elucidation and modulation of active sites in holey graphene electrocatalysts for H₂O₂ production, *EcoMat* 5 (2023), e12266.
- [42] K. Lee, J. Lim, M.J. Lee, K. Ryu, H. Lee, J.Y. Kim, H. Ju, H.-S. Cho, B.-H. Kim, M. C. Hatzell, J. Kang, S.W. Lee, Structure-controlled graphene electrocatalysts for high-performance H₂O₂ production, *Energy Environ. Sci.* 15 (2022) 2858–2866.
- [43] C. Xia, Y. Xia, P. Zhu, L. Fan, H. Wang, Direct electrosynthesis of pure aqueous H₂O₂ solutions up to 20% by weight using a solid electrolyte, *Science* 366 (2019) 226–231.
- [44] S. Li, S. Wang, M.M. Salamone, A.W. Robertson, S. Nayak, H. Kim, S.C.E. Tsang, M. Pasta, J.H. Warner, Edge-enriched 2D MoS₂ thin films grown by chemical vapor deposition for enhanced catalytic performance, *ACS Catal.* 7 (2017) 877–886.
- [45] Y. Yan, Y. Gao, H. Zheng, B. Yuan, Q. Zhang, Y. Gu, G. Zhuang, Z. Wei, Z. Yao, X. Zhong, X. Li, J. Wang, Simultaneous electrochemical ozone production and hydrogen evolution by using tantalum-based nanorods electrocatalysts, *Appl. Catal. B* 266 (2020), 118632.
- [46] S. Zhang, H. Zhuo, S. Li, Z. Bao, S. Deng, G. Zhuang, X. Zhong, Z. Wei, Z. Yao, J.-g Wang, Effects of surface functionalization of mxene-based nanocatalysts on hydrogen evolution reaction performance, *Catal. Today* 368 (2021) 187–195.
- [47] J. Wang, B. Guo, J. Sun, Y. Zhou, C. Zhao, Z. Wei, J. Guo, Cooperative hydrogen evolution reaction combining Cu₂₊₁O and Ru active sites, *Appl. Catal. B* 324 (2023), 122169.
- [48] J. Wei, D.S. Xia, Y.P. Wei, X.Y. Zhu, J. Li, L. Gan, Probing the oxygen reduction reaction intermediates and dynamic active site structures of molecular and pyrolyzed Fe-N-C electrocatalysts by In Situ Raman spectroscopy, *ACS Catal.* (2022) 7811–7820.
- [49] J.C. Dong, M. Su, V. Briega-Martos, L. Li, J.B. Le, P. Radjenovic, X.S. Zhou, J. M. Feliu, Z.Q. Tian, J.F. Li, Direct In Situ Raman spectroscopic evidence of oxygen reduction reaction intermediates at high-index Pt (hkl) surfaces, *J. Am. Chem. Soc.* 142 (2020) 715–719.
- [50] Y.H. Wang, J.B. Le, W.Q. Li, J. Wei, P.M. Radjenovic, H. Zhang, X.S. Zhou, J. Cheng, Z.Q. Tian, J.F. Li, In situ spectroscopic insight into the origin of the enhanced performance of bimetallic nanocatalysts towards the oxygen reduction reaction (ORR), *Angew. Chem. Int. Ed.* 58 (2019) 16062–16066.
- [51] J.-C. Dong, X.-G. Zhang, V. Briega-Martos, X. Jin, J. Yang, S. Chen, Z.-L. Yang, D.-Y. Wu, J.M. Feliu, C.T. Williams, Z.-Q. Tian, J.-F. Li, In situ Raman spectroscopic evidence for oxygen reduction reaction intermediates at platinum single-crystal surfaces, *Nat. Energy* 4 (2019) 60–67.
- [52] J. Zhang, J. Ma, T.S. Choksi, D. Zhou, S. Han, Y.F. Liao, H.B. Yang, D. Liu, Z. Zeng, W. Liu, X. Sun, T. Zhang, B. Liu, Strong metal-support interaction boosts activity, selectivity, and stability in electrosynthesis of H₂O₂, *J. Am. Chem. Soc.* 144 (2022) 2255–2263.
- [53] Z.-T. Hu, Y.N. Liang, J. Zhao, Y. Zhang, E.-H. Yang, J. Chen, T.-T. Lim, Ultra-effective integrated technologies for water disinfection with a novel 0D–2D–3D nanostructured rGO-AgNP/Bi₂Fe₂O₉ composite, *Appl. Catal. B* 227 (2018) 548–556.
- [54] Z.-T. Hu, Y. Chen, Y.-F. Fei, S.-L. Loo, G. Chen, M. Hu, Y. Song, J. Zhao, Y. Zhang, J. Wang, An overview of nanomaterial-based novel disinfection technologies for harmful microorganisms: mechanism, synthesis, devices and application, *Sci. Total Environ.* 837 (2022), 155720.